Journal of Magnetic Resonance 194 (2008) 99–107

Contents lists available at ScienceDirect

Journal of Magnetic Resonance

journal homepage: www.elsevier.com/locate/jmr

# Optimal *k*-space sampling for single point imaging of transient systems

Prodromos Parasoglou [a], A.J. Sederman [a], J. Rasburn [b], H. Powell [b], M.L. Johns [a,*]

[a] Department of Chemical Engineering, University of Cambridge, New Museums Site Pembroke Street, Cambridge CB2 3RA, UK
[b] Nestec York Ltd., Nestlé Product Technology Centre, Haxby Road, PO Box 204, York YO91 1XY, UK

ARTICLE INFO

*Article history:*
Received 28 April 2008
Revised 12 June 2008
Available online 20 June 2008

*Keywords:*
*k*-space
SPI
Selective sampling
Rapid imaging

ABSTRACT

A novel approach for sampling *k*-space in a pure phase encoding imaging sequence is presented using the Single Point Imaging (SPI) technique. The sequence is optimised with respect to the achievable Signal-to-Noise ratio (*SNR*) for a given time interval via selective sparse *k*-space sampling, dictated by prior knowledge of the overall object of interest's shape. This allows dynamic processes featuring short $T_2^*$ NMR signal to be more readily followed, in our case the absorption of moisture by a cereal-based wafer material. Further improvements in image quality are also shown via the use of complete sampling of *k*-space at the start or end of the series of imaging experiments; followed by subsequent use of this data for un-sampled *k*-space points as opposed to zero filling.



## 1. Introduction

Single point imaging (SPI) techniques [1,2], employing pure phase encoding, have proved very effective for imaging materials where the transverse relaxation times ($T_2^*$) are very short, typically 50–300 μs [3]. By comparison, frequency encoded imaging techniques require a minimum time (typically of the order of a ms) for the formation of an echo, thus limiting their ability to image very short $T_2$ samples. SPI has been used successfully to image a range of materials ranging from semi-crystalline polymers [4,5] to cement [6]. A significant limitation of this technique is the long acquisition times required, often dictated by hardware limitations due to gradient switching. Balcom and co-workers have significantly overcome this limitation via development of the SPRITE pulse sequence [7], in which the required phase encoding gradients are ramped up in discrete steps. Additional improvements (ultimately in speed of image acquisition) implemented by Balcom and co-workers include the acquisition of several points in the FID (and hence several separate images), followed by rescaling of spatial resolution using a chirp z-transform such that the images could be co-added [8,9]. Another improvement to the basic SPI technique has been proposed by Nauerth [10], in which pyramidal instead of linear ramps are used, resulting in reduction of acquisition time by reducing the resting times between gradient ramps.

SPRITE imaging techniques have been successfully and quantitatively applied to a wide range of samples including polymeric materials with a $T_2^*$ as low as 40 μs [11], rocks [12–14], zeolite pellets [15], gelatine phantoms with metal implants [16] and gases [17,18]. SPI/SPRITE techniques have been applied to a variety of food products, in particular to follow comparatively low concentration moisture migration which typically is characterised by short $T_2^*$ values. In this context, confectionery [19], starch molding operations [20], rice seeds [21] and sandwiches [22] have all been studied. Spatial mapping of solid and liquid lipids in various confectionery products has also been achieved [23].

Conventionally MRI techniques use a line by line rectilinear trajectory in order to sample the entire *k*-space. Many alternative ways of sampling *k*-space have been proposed in the past, especially for medical MRI [24]. Echo Planar images (EPI) are often typically in a trajectory that begins in one corner of *k*-space and ends in the diagonally opposite corner. In some cases more complicated trajectories are used such as sinusoidal [25] or trapezoidal [26]. Spiral [27,28] and radial [29] scans have been proposed for medical imaging to reduce motion artefacts and accelerate image acquisition. In most of the methods mentioned above, *k*-space points do not fall naturally on Cartesian coordinates and hence need to be re-gridded prior to image reconstruction [30]. In the case of pure phase encoding imaging techniques similar trajectories have been used mostly for the improvement of the *SNR*. Mastikhin *et al.* [31] reported the first centric trajectory with the use of SPRITE. An additional advantage of a centric scan is the ease with which one can introduce contrast in an image ($T_1$ or $T_2$) with the right magnetization preparation [32]. Several other elegant *k*-space trajectories for pure phase encoding imaging techniques have been proposed in literature in either one [33] or more dimensions [34,35]; all of them ultimately aimed at improving the *SNR* of the final image in a given total acquisition time. All of the above mentioned trajectories make use of geometrical functions (spirals, square spirals) or slightly modified geometrical functions (such as truncated spirals

* Corresponding author. Fax: +44 1223 334796.
*E-mail address:* mlj21@cheng.cam.ac.uk (M.L. Johns).

1090-7807/$ - see front matter © 2008 Elsevier Inc. All rights reserved.
doi:10.1016/j.jmr.2008.06.005

at the extremes of ***k***-space). The speed of acquisition is often increased in these sampling strategies by not acquiring all of ***k***-space; un-acquired points are zero-filled before the required Fourier transform.

The concept of an arbitrary trajectory for ***k***-space sampling has been used for selective excitations of arbitrary shapes in a method known as Completely Arbitrary Regional Volume Excitation (CARVE) [36–38]. This method excites a predetermined shape in real space by only exciting the required points in ***k***-space. In the present study a similar principle is used in order to define the sampling trajectory.

In the work presented here, we ultimately consider moisture absorption from humidified air by a thin cereal-based wafer material. The wafer can be considered to be a starch-based foam. Such moisture absorption (and subsequent migration within the foam) occurs during a conditioning process. The conditioning process is required in order to optimise the expansion properties of the wafer for subsequent fabrication steps during confectionery production. Hence, this aspect has a significant role to play in the quality of the product.

Temporally resolved Magnetic Resonance Imaging of this moisture absorption process by the foam is extremely challenging as the porosity of the foam is typically 80–90 vol% and the absorbed moisture is typically only 2–7 wt% of the solid content. In addition, the low moisture content means that the 'bound' water has restricted mobility and the highly porous nature of the foam structure results in significant magnetic susceptibility variations. These collectively result in a short $T_2^*$ for water, typically of the order of 50 μs. Imaging of this system with conventional frequency encode methods is not possible, hence the use of single point techniques is necessitated. The moisture signal is also, however, characterised by a relatively long longitudinal relaxation time, $T_1$ (~1s). The implications of this combination of a short $T_2^*$ and a long $T_1$ will become apparent below.

To ultimately produce 3D images of the moisture absorption process, we required improvements in the sensitivity of the method in order to reduce total acquisition times. This was achieved here using a novel truncated ***k***-space sampling trajectory, based on the known shape of the sample that maximised use of the available magnetisation and thus the Signal-to-Noise ratio (*SNR*). The error associated with the extent of truncation was quantified and shown to improve on alternative sampling trajectories. In addition, in such dynamic processes, full sampling of ***k***-space is typically possible at the start and end of the process; use of this data instead of zero-filling un-sampled ***k***-space was also explored.

## 2. Background

Magnetic resonance imaging is typically performed by suitable exploitation of the following Fourier relationship between the acquired signal, $S(\boldsymbol{k})$, and the signal density, $\rho(\boldsymbol{r})$:

$$\rho(\boldsymbol{r}) = \iiint S(\boldsymbol{k}) \exp(-i2\pi k\boldsymbol{r})\, \mathrm{d}\boldsymbol{k}, \tag{1}$$

where $k = \frac{\gamma G t}{2\pi} \cdot \boldsymbol{G}$ is the strength of the applied gradient, $\gamma$ is the relevant gyro-magnetic ratio and $t$ is the effective temporal duration of gradient application.

Single point imaging (SPI), also known as constant time imaging, was introduced by Emid and Creyghton [1,2] as an imaging technique to overcome the line-width restriction of samples with reduced mobility. A typical 2D SPI pulse sequence is shown in Fig. 1. In SPI, ***k***-space is sampled one point at a time using an appropriate combination of phase-encoding gradients; consequently the time period between signal excitation and single point detection can be relatively short. Since the time evolution of the signal is not measured, the only interaction that contributes to the signal distribution is the applied gradient. This means that chemical shift, magnetic susceptibility, and dipolar quadrupolar distortions are reduced compared to frequency encoding methods [3]. SPI is not slice selective as it makes exclusive use of hard r.f. pulses; these are applied in the presence of the gradients and hence need to be sufficiently short to excite all frequencies introduced by the applied gradients. Assuming a rectangular r.f. pulse, Gravina and Cory [3] have determined limits on the duration of the pulse, $t_{pul}$, as well as the filter width, *FW*, needed to excite and receive all frequencies present when a sample has a spatial physical extent, $\Delta x$. For $n$ gradient steps, a maximum gradient strength, $G$, and a phase encode time, $t_p$ the frequency bandwidth of the r.f. pulse has to be:

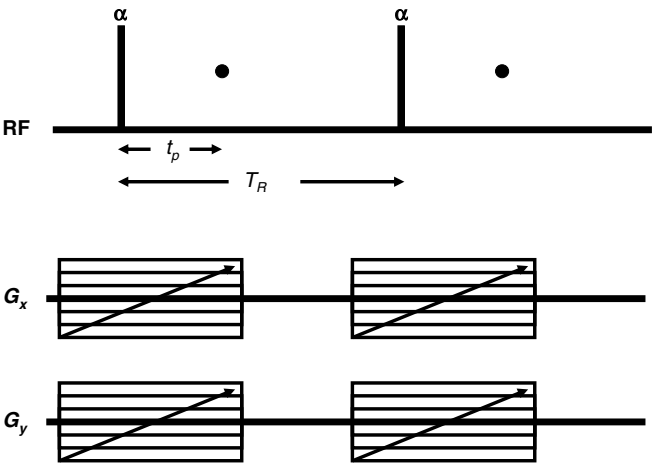


**Fig. 1.** SPI sequence in two dimensions, $x$ and $y$. A broadband rf pulse excites transverse magnetization which is phase encoded for time $t_p$. A single complex point [•] is acquired at every gradient step, $G_x$ and $G_y$. The repetition time, defined by the time between two successive rf pulses is $T_R$.

$$\Delta\nu \geqslant \frac{\gamma G \Delta x}{2\pi} = \frac{n}{2t_p}. \tag{2}$$

Since the bandwidth of a rectangular pulse is approximately the inverse of its duration:

$$t_{\mathrm{pul}} \leqslant \frac{2t_p}{n}, \tag{2}$$

and hence:

$$FW \geqslant \frac{n}{4t_p}. \tag{3}$$

As mentioned previously, SPI generally makes use of small tip angles ($\alpha$). Depending on the repetition time (*TR*), the tip angle and the value of $T_1$, SPI is a transient magnetization imaging technique. This means that the magnetization from an initial $M_0$ value will reach an equilibrium value after a certain number of pulse-acquire repetitions. Following the notation of Mastikhin et al. [31], the magnetization available for imaging after each excitation pulse, $M_n$, in the absence of magnetization preparation is:

$$M_n = M_0(1-w)C^nE^n + M_0w \tag{4}$$

where $E = \exp(-TR/T_1)$, $C = \cos(\alpha)$ and $w = \frac{1-E}{1-CE}$. Consequently each point in ***k***-space is sampled with a different amount of magnetisation, which broadens the point spread function in real space of $\rho(\mathbf{r})$ [8]. The resultant extent of image blurring will worsen for a longer $T_1$, a shorter repetition time and a larger r.f. pulse tip angle.

Short $T_1$ values (typically 10 s of ms) greatly facilitate the use of SPRITE techniques which enable, and in fact in the context of gra-

dient duty, require a short $T_R$. However with respect to a long $T_1$ (of the order of seconds), excessive blurring would occur with a relatively short $T_R$, meaning that a combination of a small tip angle and/or a relatively long $T_R$ is inevitable. Small tip angles are undesirable in terms of *SNR* delivered. Thus a long $T_R$ is required for such samples characterised by a long $T_1$, which negates the effective use of SPRITE and necessitates the use of SPI instead. This is the case for the samples considered in the work presented here where $T_1$ is approximately a second.

## 3. Technique development

The SNR ratio for an image is predominantly determined by points acquired at low $\boldsymbol{k}$ values (corresponding to lower spatial frequencies [39]). Hence more optimal use of the available magnetisation, before it reaches its equilibrium value as dictated by Eq. (4) is achieved via sampling trajectories that are initiated at the $\boldsymbol{k}$-space origin. This concept was exploited in the centric scans used for SPRITE acquisitions by Mastikhin et al. [31]. As mentioned earlier several centric trajectories have been proposed in literature [32–35]. In the work presented here, an alternative way of sampling $\boldsymbol{k}$-space is proposed that is suitable when prior knowledge of the system exists. Instead of a general geometric $\boldsymbol{k}$-space trajectory, a trajectory that maximises the *SNR* is implemented. The relatively simple principle employed is that $\boldsymbol{k}$-space points with the highest probable modulus signal intensity are acquired with the highest value of magnetisation.

The implementation of our sampling algorithm is as follows: Prior knowledge of the general outline shape of the object is required. In our case we wish to monitor moisture absorption by the starch foam. An image of the initial 'dry' sample is readily achieved using conventional SPI, acquiring all of $\boldsymbol{k}$-space, and sub-

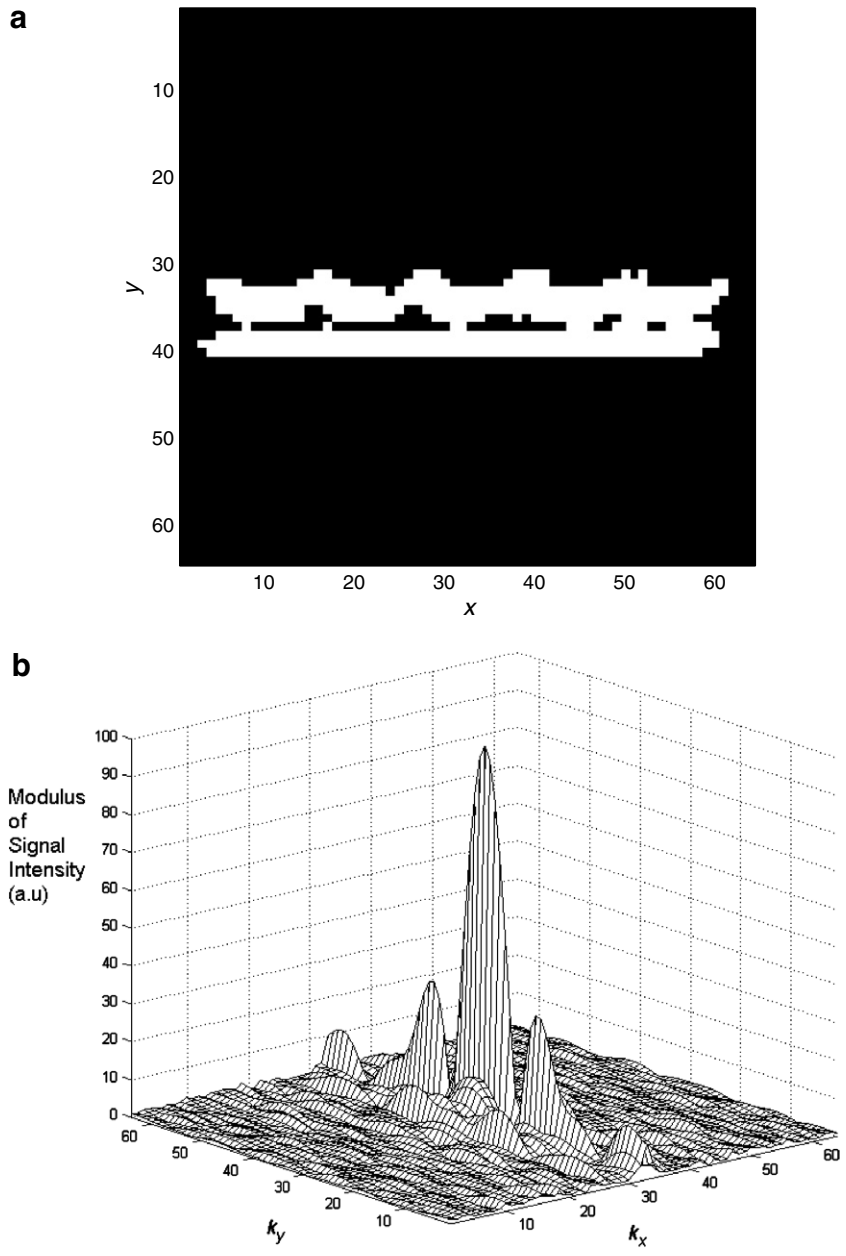


**Fig. 2.** (a) Binary gated image of the starch wafer sample, the centre of the sample is very porous and has a very low moisture signal compared to the perimeter, *x* and *y* refer to pixel number, (b) modulus of $\boldsymbol{k}$-space produced from (a).

sequently binary gated in order to study the net effect of the geometry of the system on the shape of ***k***-space—a sample binary image is presented in Fig. 2(a). This is subsequently inverse Fourier transformed into the ***k***-space domain (Fig. 2(b)). With reference to Fig. 2(b), the centre of ***k***-space is dominant, however there are also significant peaks further away from the centre. A clear limitation is the requirement that the shape of the object under study is known and that it does not vary significantly. With respect to the wafer systems studied here, structural collapse occurs at approximately 25 wt% water, which is significantly higher than the typical maximum value during industrial processing.

In the algorithm the resultant ***k***-space points (as presented in Fig. 2(b)) are sorted from the maximum to minimum value of their modulus signal, creating a rank order. Consistent with the centric scan practise [32], ***k***-space points are sampled sequentially in batches called interleafs. A time interval of $5 \times T_1$ is allowed between each interleaf to allow the magnetisation to fully recover. ***k***-space point allocation to the interleafs is done based on the rank order with higher magnetisation levels being used to acquire those points with a higher rank order. This strategy is schematically demonstrated in Fig. 3. The rank-order can then also be readily used for sparse ***k***-space sampling strategies in order to reduce total acquisition times. This is only really a sensible approach when the basic sample shape is known and the phenomenon taking place does not significantly alter or rotate the overall object shape. Although well defined rotation around the centre of ***k***-space can be compensated for [40] this is beyond the scope of, and not required by, the current study.

Whilst the above approach was implemented using SPI acquisition, in samples with shorter $T_1$ it could be readily and successfully incorporated into a SPRITE experiment. At present there are no constraints on the order of sampling ***k***-space with respect to SPI acquisition. A potentially sensible constraint that could be imposed on a SPRITE implementation would be to minimise the change in gradient strength required between successive ***k***-space point acquisitions; this would bear striking similarities with the as yet rigorously unsolved 'travelling salesman' problem [41].

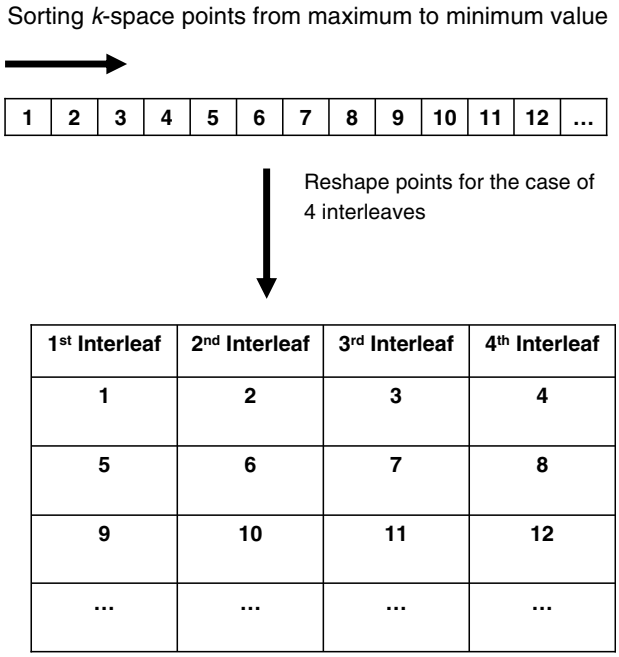


**Fig. 3.** Sorting and reshaping ***k***-space points. First all ***k***-space points are sorted according to their modulus value (top), then the global maxima will be sampled first at each interleaf (bottom).

With using sparse ***k***-space acquisition to increase acquisition speed for a series of sequentially repeated images, a further improvement in real image resolution/quality can be achieved via periodic acquisition of the full ***k***-space raster. For transient systems, such as the starch foam system studied here, such 'complete' data are readily acquired prior to or at the conclusion of the series of sequentially repeated images. In intermediate sparsely sampled images, these fully sampled data are used in preference to zero filling un-sampled ***k***-space points (hereafter referred to as a hybrid image).

## 4. Experimental

All experiments were conducted using a Bruker AV400 spectrometer equipped with a micro-imaging r.f. coil of 25 mm internal diameter. The samples were placed in a 17 mm internal diameter NMR tube featuring a glass sample holder and connected to a humidified air flow ranging from 0 to 4 ml $s^{-1}$. Samples were pieces of wafer approximately 30 mm × 17 cm × 0.3 cm wide, a photo of a sample is shown in Fig. 4 along with a schematic cross-section. SPI images of the wafer were acquired whilst humid air was blown over it. Humid air was produced by immersion of a dry air stream into a humidifying column before entering the sample tube. The air flow rate was monitored with the use of a rotameter, its temperature varied between 18.1 and 19.2 °C and the relative humidity ranged from 95% to 100%.

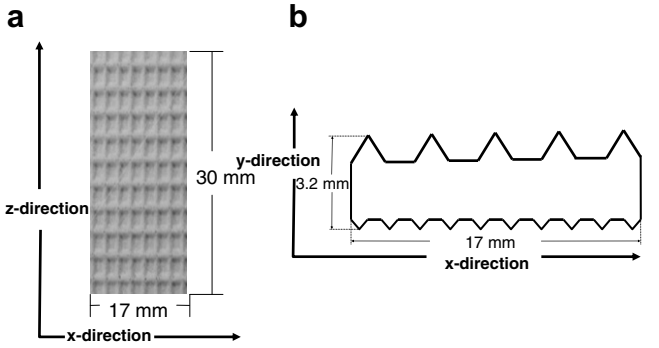


**Fig. 4.** (a) A Photo of the wafer sheet with dimensions shown. (b) Schematic representation of the reeding pattern and the dimensions of a cross-section of the foam sample. This is the orientation used for all image acquisition.

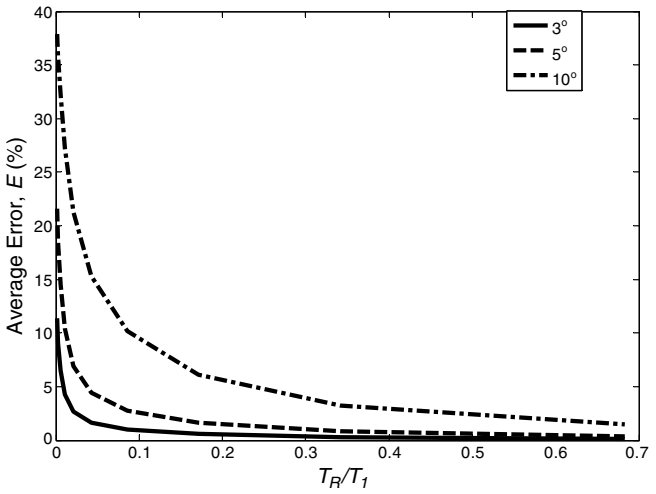


**Fig. 5.** Simulation of the average error, $E$, introduced as a function of $T_1$ and repetition time ($T_R$) for different tip angle ($\alpha$) values. For our experiments the combination of a $T_R$ of 10 ms and a tip angle of 5° correspond to an average mean error of less than 5%.

2D SPI projections of the foam were then acquired using $\alpha = 5^\circ$ corresponding to a pulse duration of 3 μs and a $T_R$ of 10 ms. The phase encoding time was 100 μs. The orientation of the 2D images of the foam were the same as the schematic in Fig. 4, perpendicular to the long axis of the wafer foam and consisted of projected signal along this axis. The images were acquired over a field of view of $2 \times 1$ cm$^2$ and consisted of $64 \times 32$ pixels, the maximum gradient strength used in both directions was 36.5 G cm$^{-1}$. For a full acquisition of ***k***-space this corresponds to a total number of points of 2048 and a total acquisition time of approximately 20 min with 16 signal averages (using 8 overleafs of 256 points each, the sampling scheme presented in Fig. 3 and 10 s between overleafs). Images were acquired as a function of moisture absorption covering the range from ~1% to 7.3% wt% moisture as determined gravimetrically (the sample was extracted at the beginning and end of the experiment and its moisture content determined using a Sartorius MA-45 moisture analyser). When sparse sampling is employed, the total acquisition time is broadly equal to the fraction of points acquired multiplied by the total original acquisition time.

## 5. Results and discussion

### 5.1. Simulation of errors

Given an original sample image and subsequently generated ***k***-space data, as presented in Fig. 2, it is possible to predict the error in a reconstructed image for a $T_1$ of 1s as a function of repetition time, $T_R$, and flip angle, $\alpha$. Error, $E$, in this study is defined as the average error of the $n$ signal-containing pixels, as follows:

$$E = \frac{\sum_1^n |X_{\text{ref}} - X|}{n}. \quad (5)$$

$X$ is the reconstructed image and $X_{\text{ref}}$ is the ideal image corresponding to complete sampling of ***k***-space and an effectively infinite $T_R$. $X_{\text{ref}}$ and $X$ are both gated to remove noise pixels and normalised to a 0–100% signal intensity range. Since in practise repetition time will not be long enough to ensure a full relaxation

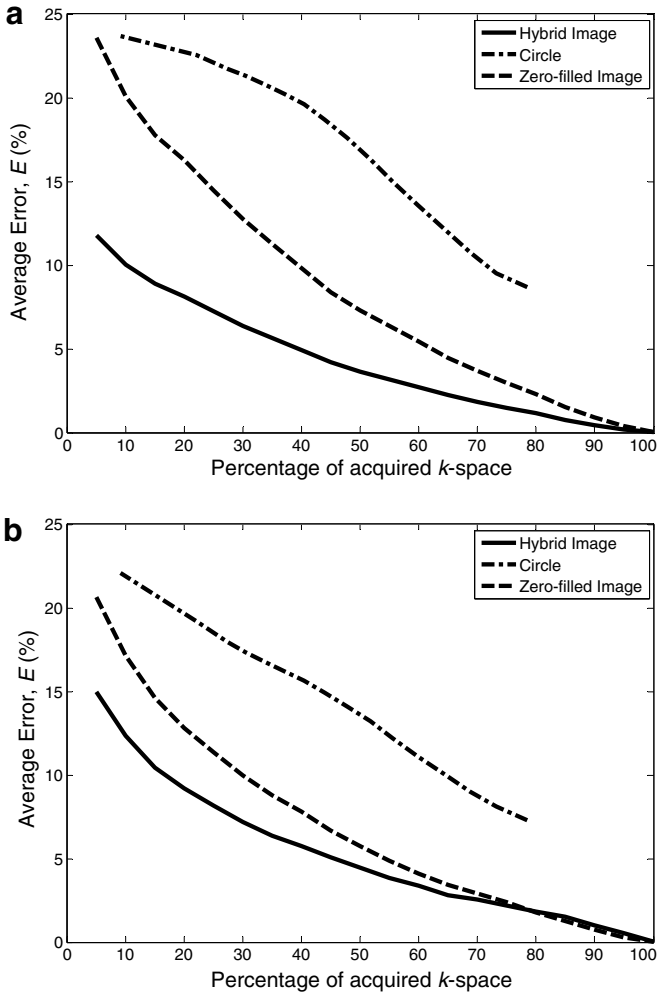


**Fig. 7.** Average error, $E$, as a function of % of ***k***-space acquired (a) scenario (i) (b) scenario (ii).

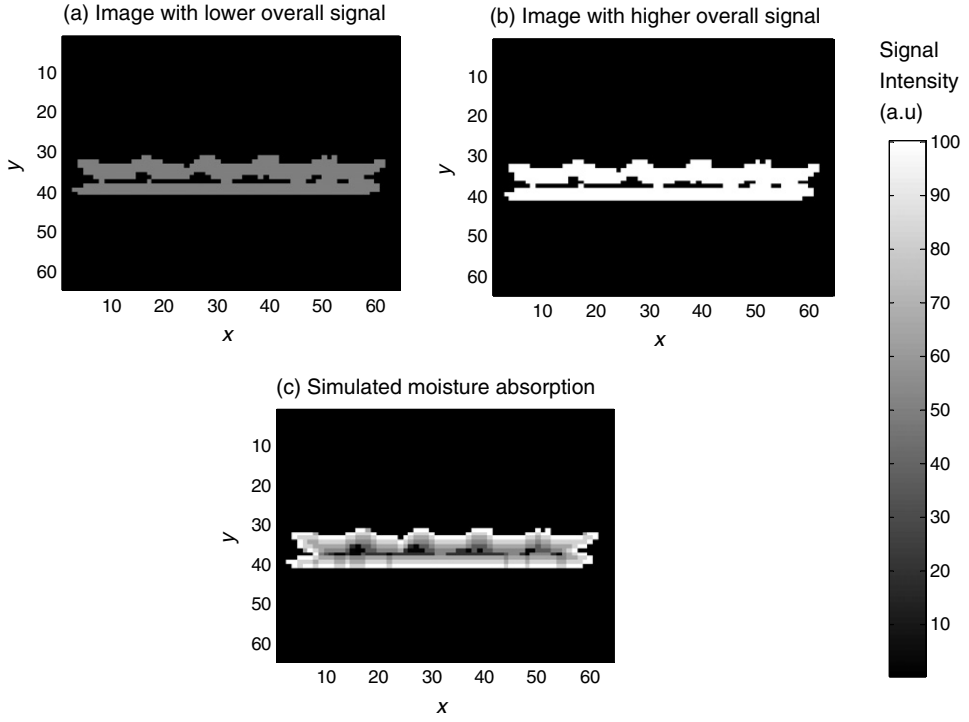


**Fig. 6.** (a) Simulated image with lower and (b) higher (bottom) overall signal. (c) Simulated image with absorbed moisture preferentially on the surface.

of the magnetization vector, this sampling method is essentially a transient magnetisation imaging technique. The resultant modulation of the magnetization will inevitably produce some blurring which will introduce a difference between $X$ and $X_{\text{ref}}$. Calculation of $E$ as a function of $T_R$, and $\alpha$ is presented in Fig. 5. As mentioned previously, all experimental images of the wafer employed $\alpha = 5°$, corresponding to a pulse duration of 3 μs, and a $T_R$ of 10 ms; with reference to Fig. 5 this corresponds to an $E$ of less than 5%. Thus $T_1$ modulation of our results was minimal.

Simulations are now presented of the average error, $E$ (as defined in Eq. (5)) as a function of the % of ***k***-space actually acquired. $X_{\text{ref}}$ is the fully sampled ***k***-space image whilst $X$ is the sparsely sampled (using our algorithm) zero-filled or hybrid image. (Model images, presented in Fig. 6 were used for this purpose.) This was bench-marked against selective acquisition of ***k***-space in an expanding circle centred at $\boldsymbol{k} = \{0,0\}$; thus proximity to the centre of ***k***-space dictated the rank order. This was done for two different model image scenarios:

(i) The binary sample image of the wafer in Fig. 2(a) was manipulated to reflect low and high even moisture distribution as shown in Fig. 6(a) and (b), respectively. Fig. 6(b) was then inverse Fourier transformed and using our algorithm the resultant error (Fig. 7) as a function of the % of ***k***-space determined.

(ii) The same procedure as (i), except that moisture absorption was assumed to occur more readily on the surface of the wafer. The resultant image is shown in Fig. 6(c).

The resultant average error, $E$, for scenario (i) for the high moisture content is shown in Fig. 7(a) as a function of the % of ***k***-space acquired. In addition, we have also included the hybrid image when the un-sampled ***k***-space points are not merely zero-filled but substituted for with the corresponding data for the original low intensity image (Fig. 6(a)). This is based on the idea that while the lower frequencies are responsible for the overall SNR of the image, the higher spatial frequencies contain information on the shape of the object and will not change significantly during the dynamic phenomenon since the geometrical shape of the object is not changing. What is evident in Fig. 7(a) is that $E$ is significantly smaller for our algorithm compared to the expanding circle. A similar plot of the error is shown in Fig. 7(b) for scenario (ii) of the simulated moisture absorption. Fig. 7(a) and (b) shows similar trends. The error in both cases remains reasonably small for significant

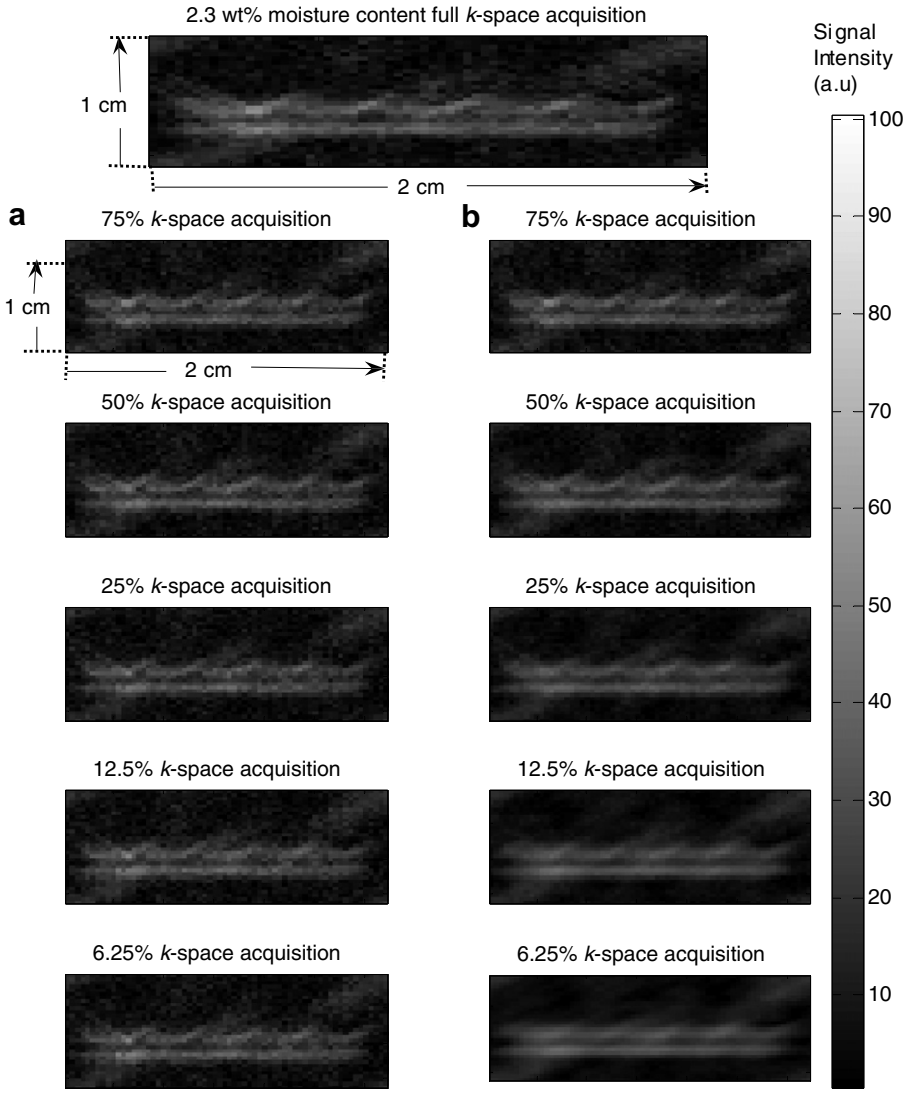


**Fig. 8.** Images of the sample with a moisture content of 2.3 (wt%). The top image is with full ***k***-space acquisition, the left column (a) shows images acquired with 75%, 50%, 25%, 12.5% and 6.25% of ***k***-space sampled, respectively, with un-sampled ***k***-space being filled with the values of the initial dry sample image (hybrid images). On the right (b) images with the same % of ***k***-space sampled, with un-sampled points filled with zeros. The pixel resolution is $312 \times 312$ μm$^2$ in all cases.

reductions in ***k***-space sampled. Sampling of 50% of ***k***-space will introduce a 5% average error in the value of the pixels. What is an acceptable error will depend almost exclusively on what is required from the acquired image. A modest improvement is observed for the hybrid image which becomes more significant as the extent of under-sampling increases.

Of course the absolute numbers presented in Fig. 7(a) and (b) will be, to some extent, sample dependant. However the trends should be consistent and the significant improvement over an imposed geometric sampling strategy retained.

### 5.2. Experimental results

Fig. 8 shows the images produced for a relatively dry sample (2.3 wt% moisture content) as a function of the % of ***k***-space acquired. The series of images acquired on the left (a) represents the hybrid images that result from using ***k***-space points of the initially dry sample for the un-sampled ***k***-space points of the comparatively wetter sample, whist the series of images on the right (b) are zero-filled. Similar data are presented in Fig. 9 for a relatively moist structure (5.8%), in this case hybridisation of the left hand side images (a) has been performed by using ***k***-space points of the final fully wet sample. Reasonable reproductions of the fully sampled image are reproduced even when only 6.25% of the ***k***-space points are acquired. The effect of hybridisation is marginal when a large portion of ***k***-space is acquired, however becomes significant when only a small fraction is sampled. A close inspection shows that fine structure in the original image is retained and not blurred as in the zero-filled cases.

Fig. 10 shows a series of images of the foam during moisture absorption from humidified air with fully acquired ***k***-space and the respective hybrid images when 50% of ***k***-space was acquired. Agreement between the images is good. The average error, *E*, was calculated as a function of moisture content and % of ***k***-space sampled and is presented in Fig. 11 for both zero-filled and hybrid images. A lower limit on *E* is created by the prevailing *SNR* of the

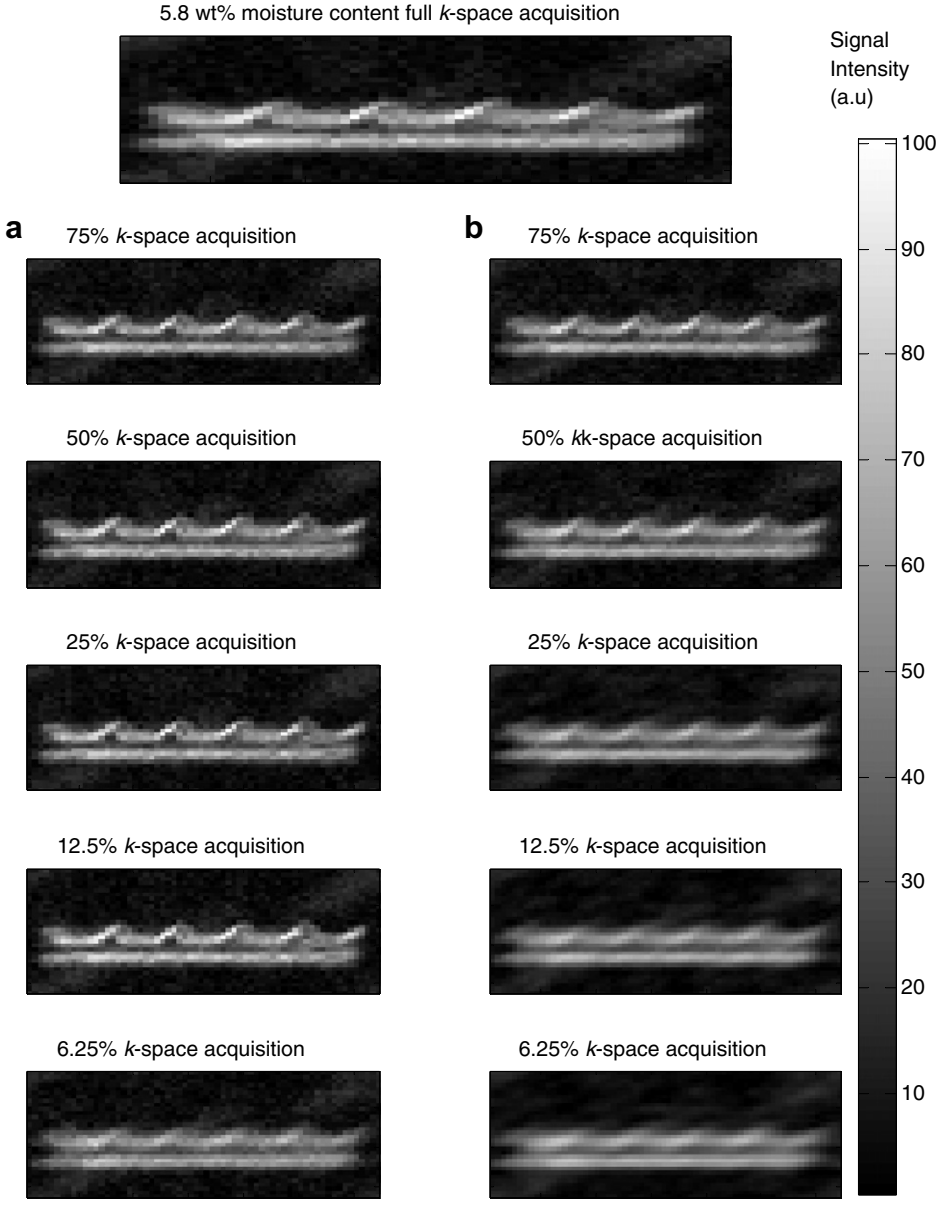


**Fig. 9.** Images of the sample with a moisture content of 5.8 (wt%). The top image is with full ***k***-space acquisition, the left column (a) shows images acquired with 75%, 50%, 25%, 12.5% and 6.25% of ***k***-space sampled, respectively, with un-sampled ***k***-space being filled with the values of the initial dry sample image (hybrid images). On the right (b) images with the same % of ***k***-space sampled, with un-sampled points filled with zeros.

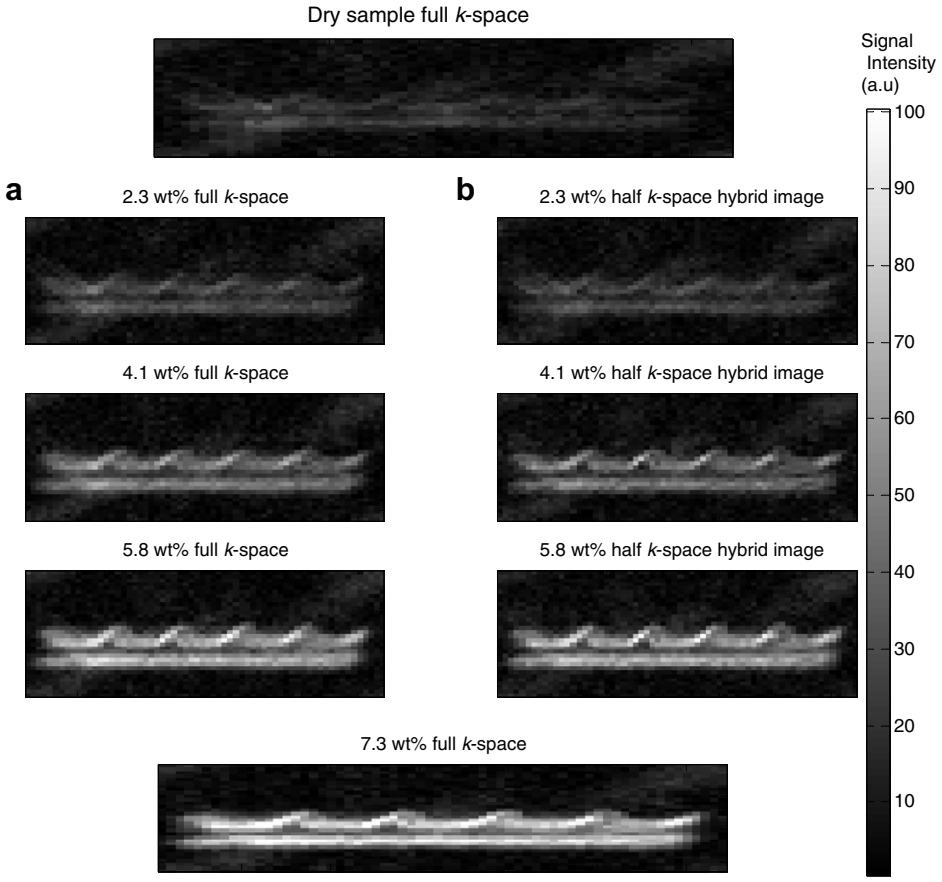


**Fig. 10.** Evolution of images for different moisture contents, the dry (top) fully acquired image and the wet (bottom) have been used to create the hybrid images at different moisture contents.

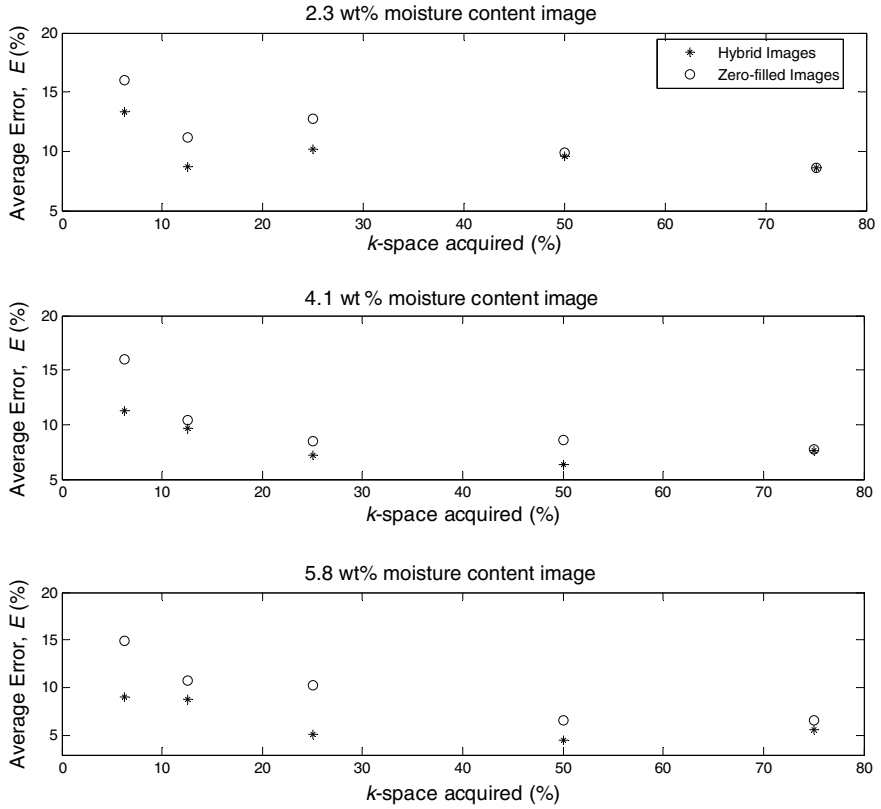


**Fig. 11.** Average error, *E*, for the sparse ***k***-space acquired images. The lower limit is dictated by the prevailing *SNR*.

respective image. This experimental data is also consequently noisier than the simulated data presented in Fig. 7. Nevertheless the trend of a modest increase in $E$ as the % of $\boldsymbol{k}$-space sampled is decreased is retained as is a slightly better performance by the hybrid images.

## 6. Conclusion

We have demonstrated that with prior knowledge of a general sample of interest's shape, a sparse $\boldsymbol{k}$-space sampling strategy in an SPI experiment can be optimised with respect to *SNR* for a given acquisition time interval. The sampling strategy employs a rank order dictated by a Fourier transform of the known general shape. Further improvement is possible for a series of sequential images by full acquisition of $\boldsymbol{k}$-space for selected images followed by substitution of these $\boldsymbol{k}$-space points, as opposed to zero-filling of unsampled points. The technique was successfully applied to 2D imaging of moisture absorption by a starch-foam sample from humidified air. In future work we will extend the strategy to 3D imaging and also account for $T_2^*$ relaxation via the acquisition (and suitable subsequent manipulation) of multiple points following each excitation. A significant requirement of the method is knowledge of the object of interest's shape; in future we will also explore the use of Bayesian analysis to determine the required $\boldsymbol{k}$-space rank order when this is not the case.

## Acknowledgments

P.P. acknowledges the financial support of Nestle and a Case Award from the BBSRC. M.L.J. acknowledges funding provided by EPSRC Grant GR/S20789/01. Helpful discussions with Prof. Bruce Balcom during a sabbatical visit is also acknowledged.

## References

[1] S. Emid, Ultra high-resolution multiple quantum spectroscopy in solids, Physica B & C 128 (1985) 79–80.
[2] S. Emid, J.H.N. Creyghton, High-resolution imaging in solids, Physica B & C 128 (1985) 81–83.
[3] S. Gravina, D.G. Cory, Sensitivity and resolution of constant-time imaging, Journal of Magnetic Resonance Series B 104 (1994) 53–61.
[4] D.E. Axelson, A. Kantzas, A. Nauerth, H-1 magnetic resonance imaging of rigid polymeric solids, Solid State Nuclear Magnetic Resonance 6 (1996) 309–321.
[5] Z.J. Fang, D. Hoepfel, K. Winter, Application of single point imaging (SPI) to solid state materials, Magnetic Resonance Imaging 19 (2001) 501–503.
[6] S.D. Beyea, B.J. Balcom, T.W. Bremner, P.J. Prado, A.R. Cross, R.L. Armstrong, P.E. Grattan-Bellew, The influence of shrinkage-cracking on the drying behaviour of White Portland cement using single-point imaging (SPI), Solid State Nuclear Magnetic Resonance 13 (1998) 93–100.
[7] B.J. Balcom, R.P. MacGregor, S.D. Beyea, D.P. Green, R.L. Armstrong, T.W. Bremner, Single-point ramped imaging with T-1 enhancement (SPRITE), Journal of Magnetic Resonance Series A 123 (1996) 131–134.
[8] M. Halse, J. Rioux, S. Romanzetti, J. Kaffanke, B. MacMillan, I. Mastikhin, N.J. Shah, E. Aubanel, B.J. Balcom, Centric scan SPRITE magnetic resonance imaging: optimization of SNR, resolution, and relaxation time mapping, Journal of Magnetic Resonance 169 (2004) 102–117.
[9] J. Kaffanke, T. Dierkes, S. Romanzetti, M. Halse, J. Rioux, M.O. Leach, B. Balcom, N.J. Shah, Application of the chirp z-transform to MRI data, Journal of Magnetic Resonance 178 (2006) 121–128.
[10] A. Nauerth, 5545991 Low-noise NMR imaging method with single point recording (SPI), Magnetic Resonance Imaging, 1997, pp. XXIII–XXIV.
[11] C.B. Kennedy, B.J. Balcom, I.V. Mastikhin, Three-dimensional magnetic resonance imaging of rigid polymeric materials using single-point ramped imaging with T-1 enhancement (SPRITE), Canadian Journal of Chemistry-Revue Canadienne De Chimie 76 (1998) 1753–1765.
[12] B.J. Balcom, J.C. Barrita, C. Choi, S.D. Beyea, D.J. Goodyear, T.W. Bremner, Single-point magnetic resonance imaging (MRI) of cement based materials, Materials and Structures 36 (2003) 166–182.
[13] P. Faure, S. Care, C. Po, S. Rodts, An MRI-SPI and NMR relaxation study of drying-hydration coupling effect on microstructure of cement-based materials at early age, Magnetic Resonance Imaging 23 (2005) 311–314.
[14] F. Marica, Q. Chen, A. Hamilton, C. Hall, T. Al, B.J. Balcom, Spatially resolved measurement of rock core porosity, Journal of Magnetic Resonance 178 (2006) 136–141.
[15] P.J. Prado, B.J. Balcom, M. Jama, Single-point magnetic resonance imaging study of water adsorption in pellets of zeolite 4A, Journal of Magnetic Resonance 137 (1999) 59–66.
[16] P. Ramos-Cabrer, J.P.M. van Duynhoven, A. Van der Toorn, K. Nicolay, MRI of hip prostheses using single-point methods: in vitro studies towards the artifact-free imaging of individuals with metal implants, Magnetic Resonance Imaging 22 (2004) 1097–1103.
[17] P.J. Prado, B.J. Balcom, I.V. Mastikhin, A.R. Cross, R.L. Armstrong, A. Logan, Magnetic Resonance Imaging of Gases: a single-point ramped imaging with T1 enhancement (SPRITE) study, Journal of Magnetic Resonance 137 (1999) 324–332.
[18] B. Newling, C.C. Poirier, Y. Zhi, J.A. Rioux, A.J. Coristine, D. Roach, B.J. Balcom, Velocity imaging of highly turbulent gas flow, Physical Review Letters 93 (2004) 154503.
[19] M.Y. Troutman, I.V. Mastikhin, B.J. Balcom, T.M. Eads, G.R. Ziegler, Moisture migration in soft-panned confections during engrossing and aging as observed by magnetic resonance imaging, Journal of Food Engineering 48 (2001) 257–267.
[20] G.R. Ziegler, B. MacMillan, B.J. Balcom, Moisture migration in starch molding operations as observed by magnetic resonance imaging, Food Research International 36 (2003) 331–340.
[21] N. Ishida, S. Naito, H. Kano, Loss of moisture from harvested rice seeds on MRI, Magnetic Resonance Imaging 22 (2004) 871–875.
[22] P. Ramos-Cabrer, J.P.M. Van Duynhoven, H. Timmer, K. Nicolay, Monitoring of moisture redistribution in multicomponent food systems by use of magnetic resonance imaging, Journal of Agricultural and Food Chemistry 54 (2006) 672–677.
[23] K. Deka, B. MacMillan, G.R. Ziegler, A.G. Marangoni, B. Newling, B.J. Balcom, Spatial mapping of solid and liquid lipid in confectionery products using a ID centric SPRITE MRI technique, Food Research International 39 (2006) 365–371.
[24] C.B. Paschal, H.D. Morris, k-space in the clinic, Journal of Magnetic Resonance Imaging 19 (2004) 145–159.
[25] T.G. Reese, J.D. Pearlman, MR gradient response modeling to ensure excitation coherence, Journal of Magnetic Resonance Imaging 4 (1994) 569–576.
[26] P.R. Harvey, P. Mansfield, Resonant trapezoidal gradient generation for use in echo-planar imaging, Magnetic Resonance Imaging 12 (1994) 93–100.
[27] C.H. Meyer, B.S. Hu, D.G. Nishimura, A. Macovski, Fast Spiral Coronary Artery Imaging, Magnetic Resonance in Medicine 28 (1992) 202–213.
[28] J.R. Liao, J.M. Pauly, N.J. Pelc, MRI using piecewise-linear spiral trajectory, Magnetic Resonance in Medicine 38 (1997) 246–252.
[29] V. Rasche, R.W. Deboer, D. Holz, R. Proksa, Continuous radial data-acquisition for dynamic MRI, Magnetic Resonance in Medicine 34 (1995) 754–761.
[30] R.M. Heidemann, M.A. Griswold, N. Seiberlich, G. Krüger, S.A. Kannengiesser, B. Kiefer, G. Wiggins, L.L. Wald, P.M. Jakob, Direct parallel image reconstructions for spiral trajectories using GRAPPA, Magnetic Resonance in Medicine 56 (2006) 317–326.
[31] I.V. Mastikhin, B.J. Balcom, P.J. Prado, C.B. Kennedy, SPRITE MRI with prepared magnetization and centric k-space sampling, Journal of Magnetic Resonance 136 (1999) 159–168.
[32] A.A. Khrapitchev, B. Newling, B.J. Balcom, Centric-scan SPRITE magnetic resonance imaging with prepared magnetisation, Journal of Magnetic Resonance 181 (2006) 271–279.
[33] I.V. Mastikhin, H. Mullally, B. MacMillan, B.J. Balcom, Water content profiles with a 1D centric SPRITE acquisition, Journal of Magnetic Resonance 156 (2002) 122–130.
[34] M. Halse, D.J. Goodyear, B. MacMillan, P. Szomolanyi, D. Matheson, B.J. Balcom, Centric scan SPRITE magnetic resonance imaging, Journal of Magnetic Resonance 165 (2003) 219–229.
[35] A.A. Khrapitchev, B. Newling, B.J. Balcom, Sectoral sampling in centric-scan SPRITE magnetic resonance imaging, Journal of Magnetic Resonance 178 (2006) 288–296.
[36] I. Sersa, S. Macura, Excitation of arbitrary shapes in nuclear magnetic resonance by a random walk in discrete k space, Journal of Magnetic Resonance Series B 111 (1996) 186–188.
[37] I. Sersa, S. Macura, Excitation of complicated shapes in three dimensions, Journal of Magnetic Resonance 135 (1998) 466–477.
[38] I. Sersa, S. Macura, Volume selective detection by weighted averaging of constant tip angle scans, Journal of Magnetic Resonance 143 (2000) 208–212.
[39] J.C. Russ, Image Processing Handbook, fourth ed., CRC Press, Inc., 2002.
[40] A.J. Sederman, K.G. Hollingsworth, M.L. Johns, L.F. Gladden, Development and application of rotationally compensated RARE, Journal of Magnetic Resonance 171 (2004) 118–123.
[41] G. Gutin, A.P. Punnen, The Traveling Salesman Problem and its Variations, Kluwer Academic Publishers, Norwell, MA, 2002.